Silicon Photonics-based Mach-Zehnder Interferometer Platform

MOHAMMAD JAVAD HAJI NAJAFI[1,2,*]

[1] *Biodesign Center for Biosensors and Bioelectronics, Arizona State University, Tempe, Arizona 85287, United States*
[2] *School of Electrical, Computer and Energy Engineering, Arizona State University, Tempe, Arizona 85287, United States*
[*] *mjnajafi@asu.edu*

Abstract: We present a simple, reusable silicon photonics platform based on a fully etched 500×220 nm strip waveguide and unbalanced Mach–Zehnder interferometers (MZIs) designed for operation around 1550 nm. The circuit integrates four MZIs with path-length differences $\Delta L = \{50, 100, 150, 200\}$ µm and a grating-coupler-to-grating-coupler reference for loopback calibration. On the modelling side, we use Lumerical MODE/INTERCONNECT to extract a compact polynomial for the effective index, derive the MZI transfer function, and predict the free spectral range (FSR) and group index. On the experimental side, we implement a measurement flow combining GC–GC loopback calibration, baseline correction, autocorrelation-based FSR estimation, and nonlinear fitting of the MZI spectrum. For the largest imbalance, $\Delta L = 200$ µm, we measure $\text{FSR}_{\text{exp}} \approx 2.82$ nm at 1550 nm, in close agreement with the simulated $\text{FSR}_{\text{sim}} \approx 2.86$ nm. The fitted polynomial yields a group index $n_g(1550 \text{ nm}) \approx 4.18$, consistent with the simulated $n_g \approx 4.20$ and with a nine-corner (H, W) process analysis. The resulting waveguide model is directly usable in circuit simulators, and the same MZI array provides a convenient tool for process monitoring and future sensing or tunable-filter implementations.

1. Introduction

Silicon photonics has matured into a versatile platform for dense, low-power optical circuits that leverage CMOS manufacturing to integrate sources, routing, modulation, and detection on compact chips [1, 2]. Among the canonical building blocks, the Mach–Zehnder interferometer (MZI) is especially valuable because it converts small phase variations into measurable intensity changes and thereby underpins tunable filters, switches, modulators, spectrometers, and label-free sensors [1, 3]. Practical silicon implementations typically combine single-mode strip or rib waveguides with compact splitters/combiners (e.g., Y-branches or multimode-interference couplers) and vertical fiber grating couplers for low-cost packaging and wafer-level testing [1]. By deliberately introducing a path-length mismatch, an *unbalanced* MZI yields a periodic transfer function with free spectral range (FSR) set by the waveguide group index and the arm length difference, enabling accurate extraction of dispersion and loss as well as straightforward wavelength referencing [2].

Beyond communications, interferometric readout on silicon has proven powerful for metrology and sensing. Changes in cladding refractive index, surface loading, temperature, or carrier density perturb the effective index and hence the MZI phase, allowing quantitative measurements of environmental and material properties with high sensitivity and low footprint [3]. When paired with simple heaters or PN/PNN junctions, the same structure forms a tunable element whose π-phase metrics (P_π for thermo-optic, $V_\pi L_\pi$ for electro-optic) directly benchmark process and device performance. Multiport layouts further support balanced detection and quadrature tracking for robust phase unwrapping, while bend-rich routing provides opportunities to quantify propagation and bend losses across fabrication corners [1, 2].

In this work, we present a compact, reusable unbalanced MZI implemented in a standard silicon photonics stack. We (i) describe the layout choices that trade off footprint, loss, and

FSR; (ii) derive and use the MZI transfer function to provide quick-look formulas for FSR and extinction; (iii) outline measurement procedures to extract group index, splitter balance, and waveguide/bend loss from simple wavelength sweeps across the multiple output ports; and (iv) discuss straightforward extensions—adding localized heaters or PN phase shifters—to convert the same test vehicle into a tunable filter/modulator and a label-free refractometric (*may be added in future report*). Together, these results offer a general, fabrication-friendly platform for education, process control, and application-driven prototyping on silicon photonics.
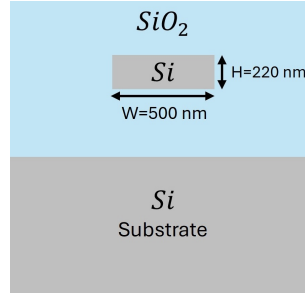

Fig. 1. 500*220 nm waveguide geometry.

2. Theory

2.1. Waveguide model

A common starting point is a single-mode strip waveguide on silicon-on-insulator (SOI) with 220 nm top silicon in most common cases, and a width near 500 nm (Fig.1). This geometry supports a quasi-TE mode around 1550 nm.

Let $n_{\text{eff}}(\lambda)$ be the effective index and $n_g(\lambda)$ the group index. By definition,

$$n_g(\lambda) = n_{\text{eff}}(\lambda) - \lambda \frac{dn_{\text{eff}}}{d\lambda}. \tag{1}$$

A compact polynomial around 1.55 µm is convenient for circuit simulation:

$$n_{\text{eff}}(\lambda \,[\mu\text{m}]) \approx n_1 + n_2(\lambda - 1.55) + n_3(\lambda - 1.55)^2. \tag{2}$$

Using the Lumerical Mode the values for a 500×220 nm TE_0 mode are:

$$n_1 = 2.444, \quad n_2 = -1.130, \quad n_3 = -0.042, \tag{3}$$

2.2. Interferometer transfer function

For ideal 50:50 splitters/combiners and identical waveguide properties in both arms (lossless form), the normalized intensity at the output of an unbalanced MZI is [1]:

$$T_{\text{MZI}}(\lambda) = \frac{1}{2} \left[1 + \cos(\beta(\lambda)\,\Delta L)\right], \tag{4}$$

with propagation constant $\beta(\lambda) = 2\pi n_{\text{eff}}(\lambda)/\lambda$ and path-length difference ΔL. A lossy version replaces $\beta \Delta L$ by $\beta \Delta L - j\alpha \Delta L/2$ to include waveguide attenuation α (power units).

Furthermore, if the two arms have propagation lengths L_1 and L_2, the normalized power transmission as a function of wavelength λ can be written as:

$$T_{\text{MZI}}(\lambda) = \frac{1}{4} \left| e^{-i\beta(\lambda)L_1} + e^{-i\beta(\lambda)L_2} \right|^2, \tag{5}$$

It is convenient to express the result in terms of the arm-length imbalance $\Delta L \equiv L_2 - L_1$. Without loss of generality we may choose the reference arm to be zero length ($L_1 = 0$), which yields the compact [1, 2]:

$$T_{\mathrm{MZI}}(\lambda) = \frac{1}{4} \left| 1 + e^{-i\beta(\lambda)\,\Delta L} \right|^2 . \tag{6}$$

For plots in decibels, the linear transmission is converted as

$$T_{\mathrm{MZI,dB}}(\lambda) = 10 \log_{10}\left(T_{\mathrm{MZI}}(\lambda)\right). \tag{7}$$

2.3. Free spectral range (FSR) and group index

Assuming weak dispersion across one period, the FSR in wavelength units is:

$$\mathrm{FSR}(\lambda) \approx \frac{\lambda^2}{n_g(\lambda)\,\Delta L}. \tag{8}$$

From a measured MZI spectrum, a first-order estimator for the group index is:

$$\hat{n}_g(\lambda) \approx \frac{\lambda^2}{\Delta L\,\mathrm{FSR}(\lambda)}. \tag{9}$$

If FSR varies with λ, a small correction is:

$$\hat{n}_g(\lambda) \approx \frac{\lambda^2}{\Delta L\,\mathrm{FSR}} - \frac{\lambda^3}{\Delta L}\frac{1}{\mathrm{FSR}^2}\frac{d\,\mathrm{FSR}}{d\lambda}. \tag{10}$$

3. Modelling and simulation

In this section, we will show the plots and tables generated from Lumerical/MATLAB/INTERCONNECT.

Waveguide geometry and polarization

Fig.2 shows the rectangular strip waveguide's TE mode provided in Fig.1 with the width = 500 nm and the height = 220 nm. Quasi-TM$_0$ may be used in the future as it would be a good option for evanescent field-based sensing.
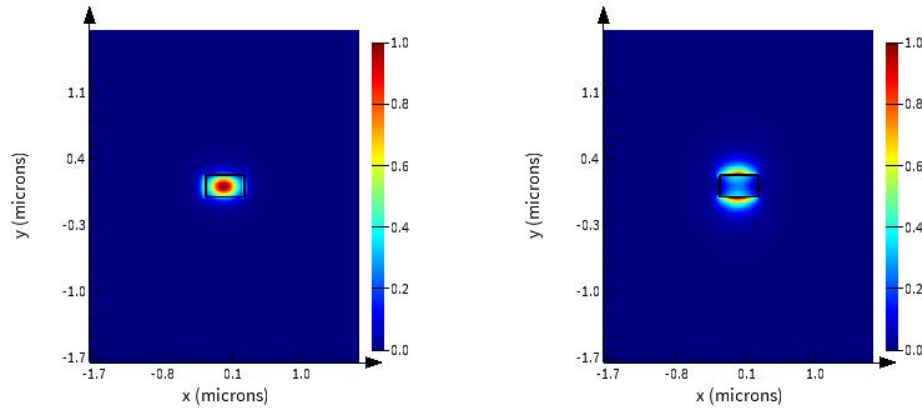

Fig. 2. Simulated waveguide mode profile: quasi-TE$_0$ (left) and quasi-TM$_0$ (right) at 1550 nm.
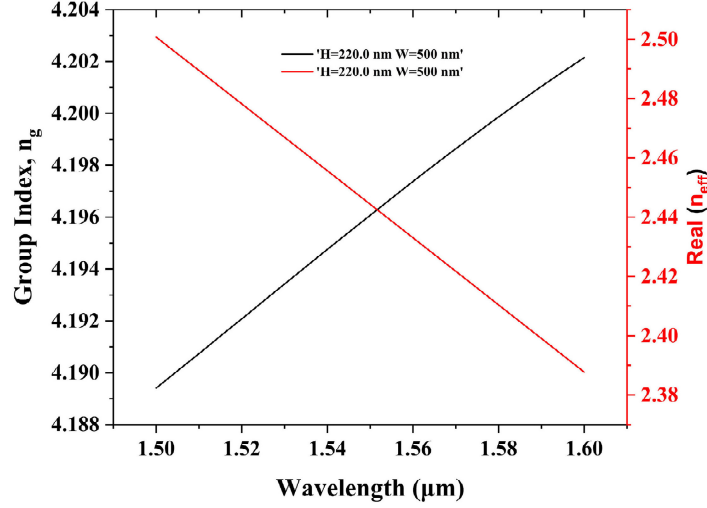
Fig. 3. Simulated effective and group index of the waveguide for the quasi-TE$_0$ mode

Effective and group index of the waveguide

Fig.3 illustrates the effective index and group index of the waveguide for the quasi-TE$_0$ mode.

INTERCONNECT simulation of the proposed silicon photonics circuit

Fig.4 shows the schematic of the proposed structure in the Lumerical INTERCONNECT and the corresponding layout. The layout depicts an unbalanced Mach–Zehnder interferometer (MZI) featuring three grating couplers, a Y-branch, and a directional coupler [4]. In the diagram, the top grating represents the input, the middle grating represents output 1, and the bottom grating represents output 2. This device serves as a versatile test vehicle and sensor: sweeping a laser yields fringes for extracting group index, propagation and bend loss, splitter and coupler balance, and wafer-level process metrics; with simple heaters or PN junctions added to one arm, it becomes a tunable filter/modulator for phase and intensity control. The same interferometric phase sensitivity enables label-free refractive index or label-free biosensing, while multiple output ports support robust quadrature readout and coherent photonics experiments. The performance of the circuit can be optimized by adjusting the geometry parameters and selecting devices for sensing purposes. Fig.5 shows the transmission spectrum of the outputs. To improve sensing performance, the circuit can be optimized (ΔL) to have a sharper transmission spectrum around 1550 nm, and polarization can be changed to TM polarization to have a higher penetration depth compared to TE polarization in order to have higher sensitivity [3, 5, 6]. In upcoming updates, I will create new circuits, test and verify them for sensing, as the presented design is merely a test design.

Parameter sweep and quick FSR sanity check

Assuming $\lambda_0 = 1.55\,\mu m$ and $n_g \approx 4.196$ (from the MODE simulation). Table 1 lists expected (from the equation 8) FSR values for common ΔL.

Group-index extraction from MZI data

Using the INTERCONNECT, we extract FSR(λ) of the model provided in Fig.4. Then we can compute $\hat{n}_g$ via Eq. (9) and compare with the waveguide model. As can be seen in Table 2, the
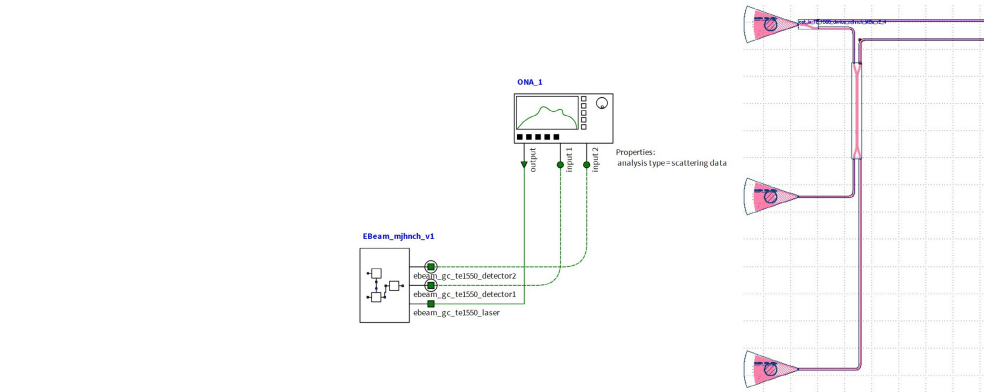
Fig. 4. Proposed MZI-based Silicon Photonics circuit (left) and the corresponding layout ($\Delta L = 200um$).
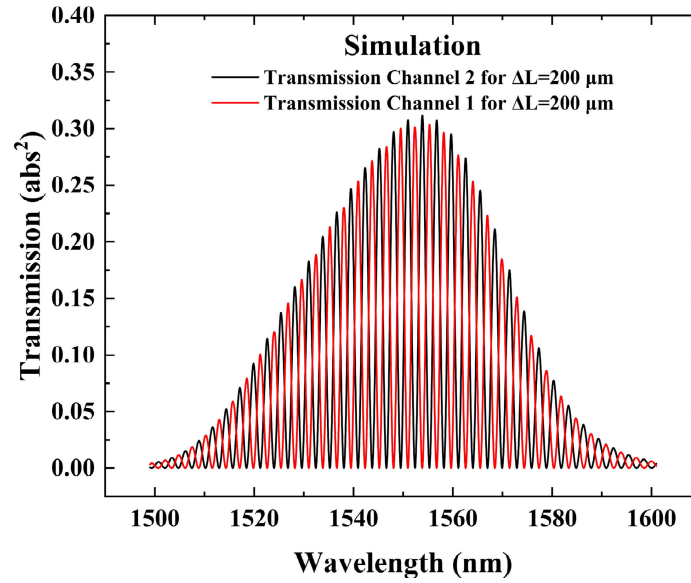

Fig. 5. Transmission spectrum of the unbalanced MZI (quasi-TE), $\Delta L = 200um$.

Table 1. Expected FSR at 1550 nm for several path mismatches (assuming n_g=4.196).

ΔL (µm)	50	100	150	200
FSR (nm)	11.45	5.73	3.82	2.87

measured $\hat{n}_g$ are close to 4.2, which is the group index of the 500×220 nm waveguide. The final layout for fabrication for this course is provided in Fig.6.

Table 2. Measured group index at 1550 nm for several path mismatches.

ΔL (µm)	50	100	150	200
Measured FSR (nm) Middle GC	11.47	5.76	3.81	2.85
Measured FSR (nm) Lower GC	11.93	5.88	3.91	2.87
Measured n_g Middle GC	4.19	4.17	4.20	4.21
Measured n_g Lower GC	4.03	4.09	4.10	4.19

3.1. Final layout: four MZIs and a GC–GC calibration path

To experimentally verify the dependence of free spectral range (FSR) on the path-length difference, the fabrication layout now contains *four* unbalanced MZIs sharing the same 500×220 nm strip waveguide platform and grating-coupler (GC) I/O. The differential path lengths are

$$\Delta L \in \{50,\ 100,\ 150,\ 200\}\ \mu m,$$

implemented by serpentine sections in one arm of each interferometer. In addition, a *GC-to-GC straight reference* is included on the same die (identical bends/routing class) to measure instrumental insertion loss (primarily GC coupling plus short-routing loss) for spectrum normalization. Figure 6 shows the full die; Figure 7 presents the spectrums to be reported including the calibration loss spectrum and the simulation results for each MZI with different ΔL.
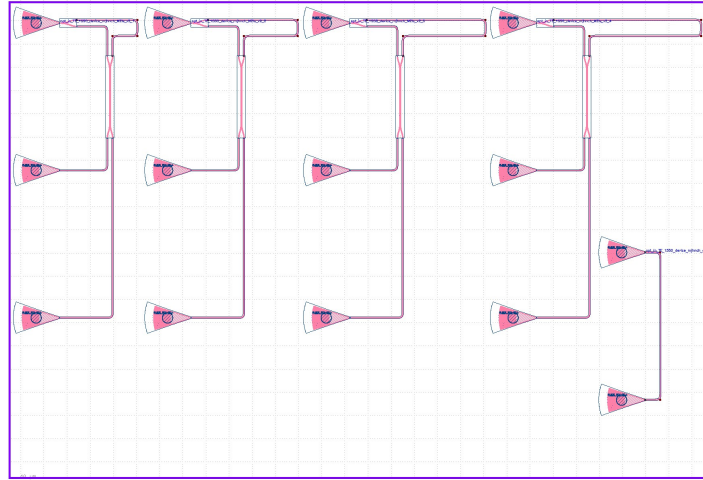

Fig. 6. Fabrication-ready layout with four unbalanced MZIs ($\Delta L = \{50, 100, 150, 200\}$ µm) and a GC–GC straight calibration path.

3.2. Anticipated trends and sanity checks

Using Eq. (8) with $n_g \approx 4.196$ at 1550 nm, the expected FSRs are:

$$\text{FSR} \approx \{11.45, \ 5.73, \ 3.82, \ 2.87\} \, \text{nm} \quad \text{for} \quad \Delta L = \{50, 100, 150, 200\} \, \mu\text{m},$$

respectively. A linear fit of FSR^{-1} versus ΔL should yield a slope of n_g/λ^2; deviations indicate dispersion, fabrication offsets in ΔL, or effective-index changes from bends and cladding variations.
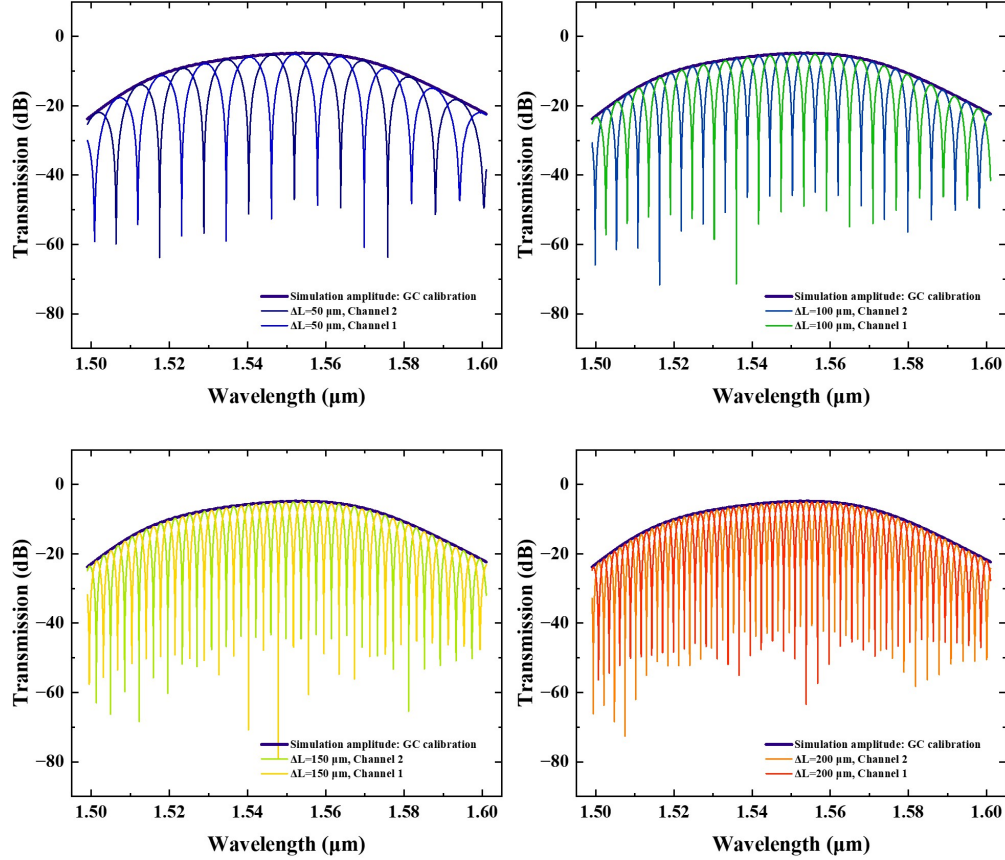

Fig. 7. (Fig. 7) GC–GC calibration or insertion-loss of GC to GC spectrum used to normalize all measurements can be seen in all images with MZI spectrums for $\Delta L = 50, 100, 150, 200 \, \mu\text{m}$.

3.3. Planned reporting

In the *Experimental data* section, we will (i) present the raw and normalized spectra for all five structures (GC–GC, four MZIs), (ii) tabulate the measured FSR and the inferred $\hat{n}_g$ from Eq. (9), and (iii) compare to the MODE-derived n_g and the predictions in Table 1. Any systematic offsets will be discussed in terms of dispersion, fabricated ΔL, and splitter imbalance.

3.4. Corner Analysis of Waveguide Geometry (H, W)

We analyzed nine process corners defined by silicon height H and waveguide width W:

Col.	Corner	Col.	Corner
1	H = 215.3 nm, W = 470 nm	6	H = 220.0 nm, W = 510 nm
2	H = 215.3 nm, W = 500 nm	7	H = 223.1 nm, W = 470 nm
3	H = 215.3 nm, W = 510 nm	8	H = 223.1 nm, W = 500 nm
4	H = 220.0 nm, W = 470 nm	9	H = 223.1 nm, W = 510 nm
5	H = 220.0 nm, W = 500 nm		

The following numerical arrays were used: wavelength, $\Re\{n_{\text{eff}}\}$, $\Im\{n_{\text{eff}}\}$, and n_g (group index). All arrays are $N \times 9$ with columns matching the corner order above.

3.4.1. Interpolation Procedure

To compare corners on a common spectral grid and to guarantee inclusion of the design wavelength, we performed a shape-preserving interpolation:

1. Convert the original wavelength vector to nanometers, λ_{nm}.

2. Build a uniform grid $\lambda_{\text{nm}}^{\star}$ with N points spanning $\min(\lambda_{\text{nm}})$ to $\max(\lambda_{\text{nm}})$.

3. Force λ = 1550 nm to lie exactly on the grid (replace nearest grid point by 1550 and re-sort).

4. Interpolate each column of $\Re\{n_{\text{eff}}\}$ and n_g onto $\lambda_{\text{nm}}^{\star}$ using `pchip` to avoid overshoot and preserve monotonic trends.

3.4.2. Free Spectral Range (FSR) from Group Index

For a Mach–Zehnder interferometer with arm length difference ΔL, the FSR (in nm) is estimated from the local group index as mentioned in (8). We evaluate (8) for $\Delta L \in \{50,\ 100,\ 150,\ 200\}\ \mu$m at each corner using the interpolated $n_g(\lambda)$.

3.4.3. Plots and Figure Conventions

We generated three families of plots:

- $\Re\{n_{\text{eff}}\}$ vs. wavelength (nine traces, one per corner, Fig.8 bottom left).

- n_g vs. wavelength (nine traces, Fig.8 top).

- FSR vs. wavelength computed via (8). For each corner we plot dot markers for the four ΔL values; additionally, we provide a combined plot for all nine corners at ΔL = 200 μm (nine traces, one per corner, Fig.8 bottom right).
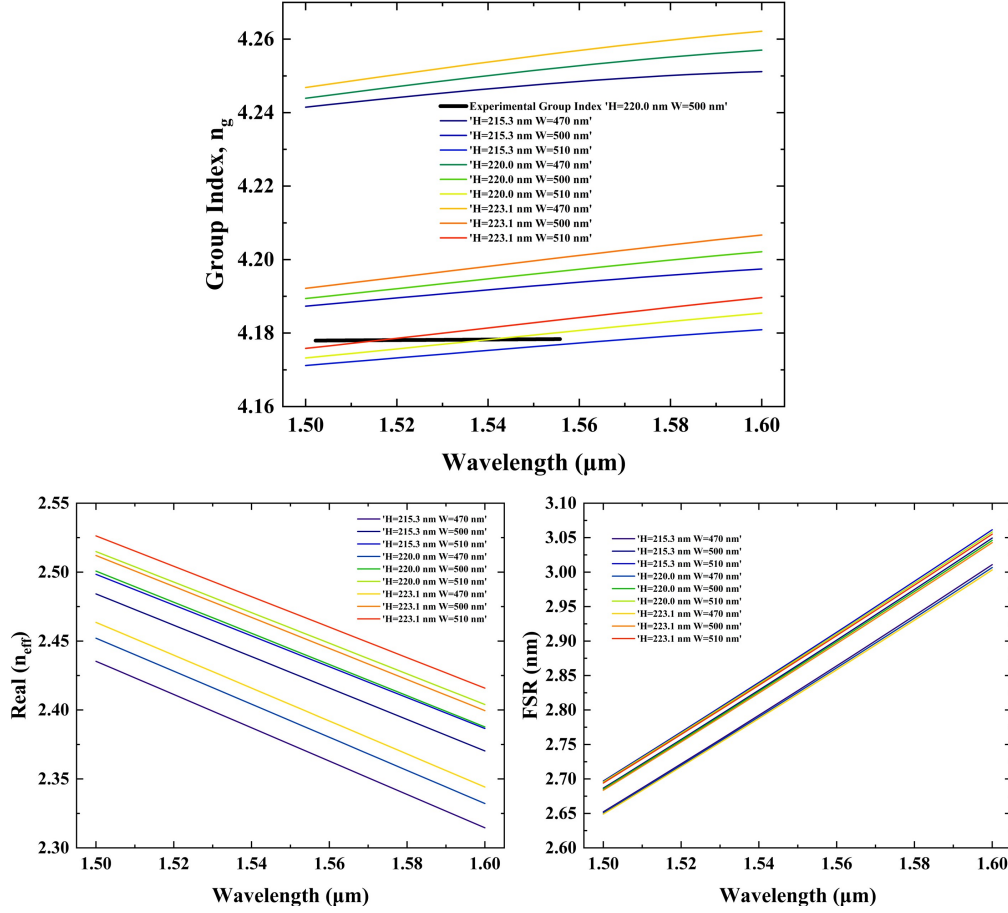
Fig. 8. Corner analysis across nine (H, W) cases. Top: interpolated n_g vs. wavelength. Bottom: interpolated $\Re\{n_{\text{eff}}\}$ and FSR vs. wavelength. Furthermore, group index extracted from the experimental results using the autocorrelation fit on the MZI with $\Delta L = 200 \, \mu m$ illustrated in the top image for ease of the comparison.

4. Fabrication

The photonic devices were fabricated using the NanoSOI MPW fabrication process by Applied Nanotools Inc. (Edmonton, Canada), which is based on direct-write 100 keV electron beam lithography technology.[1] Silicon-on-insulator wafers of 200 mm diameter, 220 nm device thickness and 2 μm buffer oxide thickness are used as the base material for the fabrication. The wafer was were pre diced into square substrates with dimensions of 25×25 mm, and lines were scribed into the substrate backsides to facilitate easy separation into smaller chips once fabrication was complete.

After an initial wafer clean using piranha solution (3:1 H_2SO_4:H_2O_2) for 15 min and water/IPA rinse, hydrogen silsesquioxane (HSQ) resist was spin-coated onto the substrate and heated to evaporate the solvent. The photonic devices were patterned using a JEOL JBX-8100FS electron beam instrument at The University of British Columbia. The exposure dosage of the design was corrected for proximity effects that result from the backscatter of electrons from exposure of nearby features. Shape writing order was optimized for efficient patterning and minimal beam

---

[1]Process description: http://www.appliednt.com/nanosoi.

drift.

After the e-beam exposure and subsequent development with a tetramethylammonium sulfate (TMAH) solution, the devices were inspected optically for residues and/or defects. The chips were then mounted on a 4 inch handle wafer and underwent an anisotropic ICP-RIE etch process using chlorine after qualification of the etch rate. The resist was removed from the surface of the devices using a 10:1 buffer oxide wet etch, and the devices were inspected using a scanning electron microscope (SEM) to verify patterning and etch quality. A 2.2 µm oxide cladding was deposited using a plasma-enhanced chemical vapour deposition (PECVD) process based on tetraethyl orthosilicate (TEOS) at 300 °C. Reflectometry measurements were performed throughout the process to verify the device layer, buffer oxide and cladding thicknesses before delivery.

5. Experimental data

5.1. Measurement set-up

To characterize the devices, a custom-built automated test setup with automated control software written in Python was used. An Agilent 81600B tunable laser was used as the input source and Agilent 81635A optical power sensors as the output detectors. The wavelength was swept from 1500 to 1600 nm in 10 pm steps. A polarization maintaining (PM) fibre was used to maintain the polarization state of the light, to couple the TE polarization into the grating couplers. A 90º rotation was used to inject light into the TM grating couplers. A polarization maintaining fibre array was used to couple light in/out of the chip.

The die contains four unbalanced MZIs with $\Delta L = \{50, 100, 150, 200\}$ µm and a straight grating-coupler-to-grating-coupler (GC–GC) reference path. For each structure, both output ports were measured. In this report we focus on the device with the largest imbalance, $\Delta L = 200$ µm, which exhibits the narrowest fringes and hence provides the highest resolution for group-index extraction.

5.2. Loopback calibration and baseline correction

The raw spectra are dominated by the finite bandwidth and spectral ripple of the grating couplers and common routing. To remove this slowly varying envelope, we use the GC–GC reference as a loopback calibration. The loopback spectrum is first fit with a fifth-order polynomial over the high-SNR region (within 14 dB of the peak). The MZI spectra are then interpolated onto the same wavelength grid and the fitted loopback polynomial is subtracted, effectively flattening the spectral envelope and leaving largely the interferometric oscillations due to the MZI.

A second, low-order (first-order) polynomial is then fit directly to each calibrated MZI spectrum and subtracted to correct any residual baseline tilt (e.g., due to residual grating slope, source drift, or long routing loss). The resulting baseline-corrected spectrum has nearly constant mean value in dB and high-contrast fringes, and is used for all subsequent analysis.

Figure 9 summarizes the key experimental spectra for the $\Delta L = 200$ µm device and compares them with the corresponding simulations. The top panels show the raw experimental MZI spectrum together with the uncalibrated simulated transfer function and the experimental loopback used for calibration. The middle panels show the simulated MZI after applying the same loopback calibration, while the bottom panels present the baseline-corrected experimental spectrum overlaid with the best-fit MZI model derived in Sec. 6.

5.3. Experimental free spectral range

For the $\Delta L = 200$ µm interferometer, the baseline-corrected spectrum exhibits periodic fringes with nearly constant free spectral range (FSR) across the measurement band. We estimate the FSR using two methods:
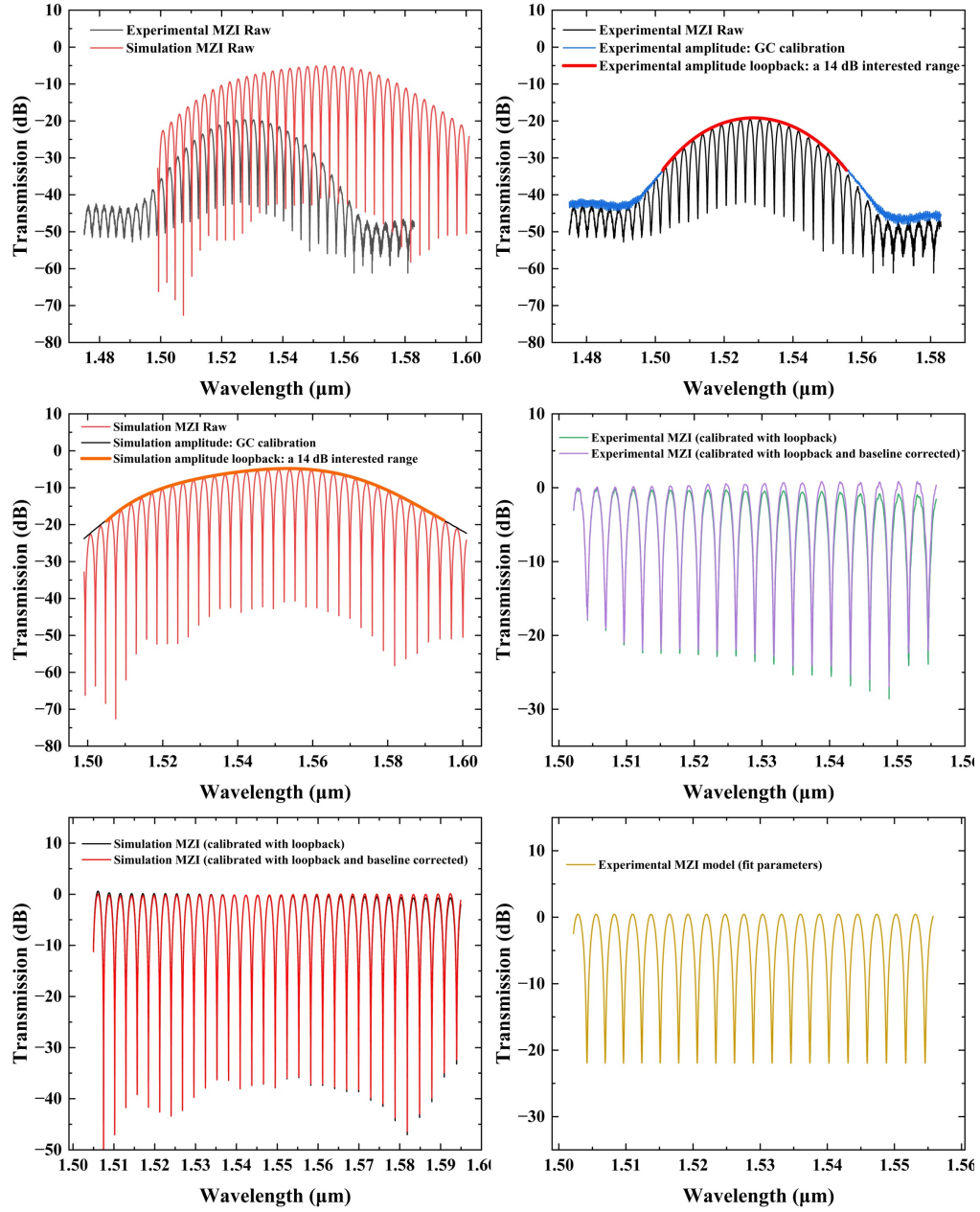
Fig. 9. Simulation–measurement comparison for the unbalanced MZI with $\Delta L = 200\,\mu\text{m}$. Top: raw experimental MZI spectrum and loopback (GC–GC) calibration curve. Middle: simulated MZI response and simulated GC calibration envelope. Bottom: calibrated experimental spectrum overlaid with the fitted MZI transfer function in dB. This figure illustrates the progressive improvement from raw data to calibrated and fitted spectra.

- Direct peak-to-peak spacing of maxima/minima using a peak-finding routine.

- Autocorrelation-based frequency estimation, in which the lag of the first non-zero peak in the autocorrelation of the spectrum gives a robust estimate of the fringe period.

The autocorrelation method is implemented in MATLAB using `xcorr` on the baseline-corrected data. From the code run provided in this work, we obtain:

$$\text{FSR}_{\text{exp}}(1550\,\text{nm}) = 2.8240 \times 10^{-9}\,\text{m} \approx 2.82\,\text{nm}, \tag{11}$$

$$n_{\text{g}}(1550\,\text{nm}) = 4.178, \tag{12}$$

where $n_{\text{g}}(1550\,\text{nm})$ is the group index at 1550 nm measured experimentally using the autocorrelation method at the nominal $\Delta L = 200\,\mu\text{m}$ (Fig. 8). The measured For comparison, the nominal MODE/INTERCONNECT simulations give $\text{FSR}_{\text{sim}} \approx 2.86\,\text{nm}$ at 1550 nm, corresponding to $n_g \approx 4.196$. The relative error between measured and simulated FSR is therefore at the 1 %–2 % level, which already indicates good agreement between design and fabrication.

6. Analysis

6.1. MZI transfer-function fit and extracted waveguide parameters

To go beyond a single FSR value and obtain a compact waveguide model, we fit the experimental MZI spectrum with the analytical transfer function of an unbalanced interferometer. The effective index is expanded as a second-order polynomial around the central wavelength λ_0 (chosen near 1.55 µm):

$$n_{\text{eff}}(\lambda\,[\mu\text{m}]) = n_1 + n_2(\lambda - \lambda_0) + n_3(\lambda - \lambda_0)^2. \tag{13}$$

The complex propagation constant is

$$\beta(\lambda) = \frac{2\pi}{\lambda}\,n_{\text{eff}}(\lambda) - j\frac{\alpha}{2}, \tag{14}$$

where α is the effective amplitude-loss coefficient. The normalized MZI power transmission in dB for path-length difference ΔL is then

$$T_{\text{MZI,dB}}(\lambda) = 10\log_{10}\left[\frac{1}{4}\,|1 + \exp(-j\beta(\lambda)\Delta L)|^2\right] + b, \tag{15}$$

where b is a constant vertical offset that accounts for the residual insertion loss after loopback calibration.

The fitting procedure proceeds in two steps:

1. **Autocorrelation-based initialization.** Using the autocorrelation of the experimental spectrum, we estimate FSR_{exp} and $n_{g,\text{av}}$. These values give a good starting guess for n_1 and n_2 and hence for the initial MZI transfer function. A cross-correlation between the experimental data and this initial model is then used to estimate any residual wavelength shift; this is converted into a small correction on n_1 so that the simulated and measured fringes are aligned.

2. **Nonlinear least-squares fit.** The corrected parameter vector $x_0 = [n_1, n_2, n_3, \alpha, b]$ is refined using MATLAB's `lsqcurvefit` routine to minimize the squared error between $T_{\text{MZI,dB}}(\lambda)$ and the experimental baseline-corrected spectrum.

For the $\Delta L = 200\,\mu\text{m}$ MZI, the final fitted parameters are

$$x_{\text{fit}} = [n_1,\,n_2,\,n_3,\,\alpha,\,b] = [2.4349,\,-1.1402,\,-0.0024,\,1.5 \times 10^{-3},\,1.0767], \tag{16}$$

with coefficient of determination

$$R^2 = 0.9930. \tag{17}$$

The excellent R^2 value confirms that the analytical MZI model with a simple second-order effective index captures the experimental spectrum very well, as also visible in Fig. 9 (bottom-right panel).

The corresponding group index at λ_0 is

$$n_{g,0} = n_1 - \lambda_0 n_2 \approx 4.1782, \tag{18}$$

which lies between the autocorrelation-based estimate $n_{g,\text{av}} = 4.1391$ and the nominal simulated value $n_g \approx 4.196$.

6.2. Comparison with simulated waveguide model and corner analysis

Table 3 compares the polynomial coefficients obtained from mode simulations (Sec. 2) with those extracted from the experimental fit.

Table 3. Polynomial waveguide model for the $500 \times 220\,\text{nm}$ TE_0 strip waveguide around 1550 nm.

Source	n_1	n_2 (μm^{-1})	n_3 (μm^{-2})
MODE simulation	2.4440	-1.1300	-0.0420
MZI fit (experiment)	2.4349	-1.1402	-0.0024

The fitted n_1 and n_2 differ from the simulated values by less than a percent, consistent with modest fabrication deviations in waveguide width/height and uncertainty in the effective path-length difference. The curvature term n_3 is significantly smaller in magnitude than in the simple MODE-based model, indicating that over the measured spectral window the dispersion experienced by the fabricated devices is slightly weaker than predicted. For most circuit-level applications the agreement is more than sufficient; the extracted model is compact and directly usable in time-domain or frequency-domain circuit simulators.

The group index obtained from the fitted coefficients is plotted as a function of wavelength and overlaid on the nine process corners in Fig. 8. The experimental curve lies close to the nominal ($H = 220\,\text{nm}, W = 500\,\text{nm}$) corner and near the centre of the bundle formed by the $\pm 5\,\text{nm}$ variations in both height and width. This confirms that the foundry process variations are well captured by the corner analysis and that the fabricated devices are close to the intended design point.

6.3. Measurement versus simulation: summary

Overall, the comparison between measurement and simulation can be summarized as follows:

- The measured FSR for $\Delta L = 200\,\mu\text{m}$ is 2.82 nm at 1550 nm, in good agreement with the simulated value of 2.86 nm.

- The waveguide polynomial coefficients extracted from the MZI :

$$(n_1, n_2, n_3) = (2.4349, -1.1402, -0.0024), \tag{19}$$

produce a group index $n_{g,0} \approx 4.18$, consistent with both the autocorrelation-based estimate and the MODE simulations.

- When overlaid on the nine-corner (H, W) analysis, the experimental group index falls within the expected spread due to ±5 nm process variations, supporting the validity of the corner models.

- The analysis pipeline—loopback calibration, baseline correction, autocorrelation-based initialization, and nonlinear fitting—provides a robust method to extract compact waveguide models from simple MZI measurements and can be directly reused for other devices and geometries.

These results demonstrate that the proposed unbalanced MZI platform is not only a useful sensing and filter building block, but also an effective process-monitoring structure for extracting waveguide parameters and validating silicon photonics fabrication runs.

7. Conclusion

In this work, we designed, fabricated, and characterized a simple and reusable silicon photonics platform based on a fully etched 500×220 nm strip waveguide and unbalanced Mach–Zehnder interferometers. On the modelling side, we built a compact polynomial description of the effective index and used it to derive the MZI transfer function, the expected free spectral range (FSR) for several arm-length imbalances, and the corresponding group index. On the experimental side, we implemented a measurement flow that uses a GC–GC loopback for spectral calibration, followed by baseline correction, autocorrelation-based frequency estimation, and nonlinear curve fitting of the MZI spectrum.

For the device with the largest path-length difference, $\Delta L = 200$ µm, the measured free spectral range around 1550 nm is $\text{FSR}_{\text{exp}} \approx 2.82$ nm, in very good agreement with the simulated value of $\text{FSR}_{\text{sim}} \approx 2.86$ nm. Using the fitted MZI model, we extract a waveguide group index at the design wavelength of

$$n_g(1550 \text{ nm}) \approx 4.18,$$

which closely matches the MODE/INTERCONNECT prediction of $n_g \approx 4.20$. Because most circuit operation and design margins are specified at 1550 nm, this wavelength-specific group index is the most relevant parameter for practical use, and it shows that the fabricated devices behave as intended within typical foundry tolerances.

The polynomial coefficients extracted from the fit,

$$(n_1, n_2, n_3) = (2.4349, -1.1402, -0.0024),$$

are consistent with the simulated values and reproduce both the FSR and the detailed fringe shape across the measurement band with $R^2 \approx 0.993$. When the resulting $n_g(\lambda)$ curve is overlaid on the nine (H, W) process corners, the experimental group index lies near the nominal $(H = 220 \text{ nm}, W = 500 \text{ nm})$ case and within the spread expected from ±5 nm variations in height and width. This confirms that the corner analysis is representative of the fabricated process and that the extracted model can be safely used in circuit-level simulations.

Beyond this specific chip, the methodology demonstrated here—loopback-based calibration, MZI-based group-index extraction at a target wavelength, and comparison against a systematic corner analysis—provides a general recipe for turning simple test structures into accurate waveguide models. The same platform can be readily extended by adding heaters or PN sections for thermo- and electro-optic tuning, by switching to the quasi-TM mode for enhanced evanescent-field sensing, or by reusing the MZI array as a process-monitoring and refractometric sensing vehicle in future silicon photonics runs.

Disclosures. The author declares no conflicts of interest.

Data Availability Statement. Data underlying the results presented in this paper will be made available upon reasonable request.

Supplemental document. This document does not have a supplemental document.

References

1. L. Chrostowski and M. Hochberg, *Silicon Photonics Design: From Devices to Systems* (Cambridge University Press, 2015).
2. W. Bogaerts and L. Chrostowski, "Silicon photonics circuit design: Methods, tools and challenges," Laser & Photonics Rev. **12**, 1700237 (2018).
3. E. Luan, H. Shoman, D. M. Ratner, *et al.*, "Silicon photonic biosensors using label-free detection," Sensors **18** (2018).
4. Z. Lu, H. Yun, Y. Wang, *et al.*, "Broadband silicon photonic directional coupler using asymmetric-waveguide based phase control," Opt. Express **23**, 3795–3808 (2015).
5. J. Flueckiger, S. Schmidt, V. Donzella, *et al.*, "Sub-wavelength grating for enhanced ring resonator biosensor," Opt. Express **24**, 15672–15686 (2016).
6. M. J. H. Najafi, S. B. Saadatmand, and S. M. Hamidi, "Ultra-high-sensitive biosensor based on srtio3 and two-dimensional materials: ellipsometric concepts," Opt. Mater. Express **12**, 2609–2622 (2022).